

1
2
3
4
5
6
7
8
9
10
11
12
13
14
15
16
17
18
19
20
21
22
23
24
25
26

**Comparison of Global Observations and Trends of Total Precipitable Water Derived
from Microwave Radiometers and COSMIC Radio Occultation from 2006 to 2013**

Shu-peng Ho¹, Liang Peng¹, Carl Mears², Richard A. Anthes¹

¹ University Corporation for Atmospheric Research, P.O. Box 3000, Boulder, CO. 80307-3000

² Remote Sensing Systems, Santa Rosa, California, USA,

Corresponding author address: Dr. Shu-Peng Ho, COSMIC Project Office, University Corporation for Atmospheric Research, P. O. Box 3000, Boulder CO. 80307-3000

E-mail: spho@ucar.edu

Manuscript for Atmospheric Chemistry and Physics

9 November 2017

Shu-Peng Ho, COSMIC Project Office, Univ. Corp. for Atmospheric Research, P. O. Box 3000, Boulder CO. 80307-3000, USA (spho@ucar.edu)

27 **Abstract**

28 We compare atmospheric total precipitable water (TPW) derived from SSM/I (Special
29 Sensor Microwave Imager) and SSMIS (Special Sensor Microwave Imager Sounder)
30 radiometers and WindSat to collocated TPW estimates derived from COSMIC
31 (Constellation System for Meteorology, Ionosphere and Climate) radio occultation (RO)
32 under clear and cloudy conditions over the oceans from June 2006 to December 2013.
33 Results show that the mean microwave (MW) radiometer - COSMIC TPW differences
34 range from 0.06-0.18 mm for clear skies, 0.79-0.96 mm for cloudy skies, 0.46-0.49 mm for
35 cloudy but non-precipitating conditions, and 1.64-1.88 mm for precipitating conditions.
36 Because RO measurements are not significantly affected by clouds and precipitation, the
37 biases mainly result from MW retrieval uncertainties under cloudy and precipitating
38 conditions. All COSMIC and MW radiometers detect a positive TPW trend over these eight
39 years. The trend using all COSMIC observations collocated with MW pixels for this data
40 set is 1.79 mm/decade, with a 95% confidence interval of (0.96, 2.63), which is in close
41 agreement with the trend estimated by the collocated MW observations (1.78 mm/decade
42 with a 95% confidence interval of 0.94, 2.62). The sample of MW and RO pairs used in
43 this study is highly biased toward middle latitudes (40° - 60° N and 40° - 65° S), and so these
44 trends are not representative of global average trends. However, they are representative of
45 the latitudes of extratropical storm tracks and the trend values are approximately four to
46 six times the global average trends, which are approximately 0.3 mm/decade. In addition,
47 the close agreement of these two trends from independent observations, which represent
48 an increase in TPW in our data set of about 6.9%, are a strong indication of the positive
49 water vapor-temperature feedback in a warming planet in regions where precipitation from

50 extratropical storms is already large.

51

52

53

54

55

56

57

58

59

60

61

62

63

64

65

66

67

68

69

70

71

72

73 **1. Introduction**

74 Clouds are important regulators for Earth's radiation and hydrological balances.
75 Water vapor is a primary variable that affects cloud radiative effects and hydrological
76 feedbacks. In addition, the three-dimensional distribution of water vapor is a key factor for
77 cloud formation and distribution (Soden et al., 2002). Held and Soden (2000) and Soden
78 and Held (2006) illustrated that water vapor amounts will increase in response to global
79 warming. Climate models predict that the column-integrated amount of water vapor, or
80 total precipitable water, will increase by $\sim 7\%$ per 1 K increase in surface temperature
81 (Wentz and Schabel, 2000; Trenberth et al., 2005; Wentz et al., 2007). Therefore, accurate
82 observations of long-term water vapor under both clear and cloudy skies are important for
83 understanding the role of water vapor on climate as well as cloud formation and
84 distribution, which is still one of the largest uncertainties in understanding climate change
85 mechanisms (IPCC 2013). Trends in global and regional vertically integrated total
86 atmospheric water vapor, or Total Precipitable Water (TPW), are important indicators of
87 climate warming because of the strong positive feedback between temperature and water
88 vapor enhancements. Accurate observations of TPW are therefore important in identifying
89 climate change and in verifying climate models, which estimate a wide range of TPW
90 trends (Roman et al. 2014).

91 The TPW depends on temperature (Trenberth and Guillemot, 1998; Trenberth et
92 al., 2005). Global TPW can be derived from satellite visible, infrared, and microwave
93 sensors (i.e., Wentz and Spencer, 1998; Fetzer et al. 2006; John and Soden, 2007; Fetzer
94 et al. 2008; Noël et al. 2004). However, no single remote sensing technique is capable of
95 completely fulfilling the needs for climate studies in terms of spatial and temporal coverage

96 and accuracy. For example, while water vapor retrievals from visible and infrared satellite
97 sensors are limited to clear skies over both land areas and oceans, passive microwave (MW)
98 imagers on satellites can provide all sky water vapor products, but only over oceans. These
99 water vapor products are mainly verified by comparing to either reanalyses, radiosonde
100 measurements, or other satellite data (i.e., Soden, and Lanzante, 1996; Sohn and Smith,
101 2003; Noël et al. 2004; Palm et al. 2008; Sohn and Bennartz, 2008; Wick et al. 2008
102 (hereafter Wick2008); Milz et al. 2009; Prasad and Singh, 2009; Pougatchev et al. 2009;
103 Knuteson et al., 2010; Larar et al. 2010; Wang et al. 2010; Ho et al. 2010a, b). Results from
104 these validation studies show that the quality of water vapor data from different satellite
105 sensors varies under different atmospheric conditions. The change of reanalysis systems
106 and inconsistent calibration among data may also cause uncertainty in long-term stability
107 of water vapor estimates. In addition, it is well known that radiosonde sensor characteristics
108 can be affected by the changing environment (Luers and Eskridge, 1998; Wang and Zhang,
109 2008). Ho et al. (2010b) demonstrated that the quality of radiosonde humidity
110 measurements varies with sensor types, adding extra difficulties in making a consistent
111 validation of long term water vapor products.

112 MW imagers are among the very few satellite instruments that are able to provide
113 long-term (close to 30 years) all-weather time series of water vapor measurements using
114 similar sensors and retrieval techniques (Wentz, 2015). The measured radiances at 19.35,
115 22.235, and 37.0 GHz from SSMIS and 18.7, 23.8, and 37.0 GHz from WindSat are used
116 to derive TPW, total cloud water (TCW), wind speed, and rainfall rates over oceans (Wentz
117 and Spencer, 1998). These four variables are retrieved by varying their values until the
118 brightness temperatures calculated using a forward model match satellite-observed

119 brightness temperatures. Because MW radiation is significantly affected (absorbed or
120 scattered) by heavy rain, these four variables are only retrieved under conditions of no or
121 light-to-moderate rain (Schlüssel and Emery, 1990; Elsaesser and Kummerow, 2008;
122 Wentz and Spencer, 1998).

123 Recently, version 7.0 daily ocean products mapped to a 0.25° grid derived from
124 multiple MW radiometers were released by Remote Sensing System (RSS) (Wentz, 2013).
125 Many validation studies have been performed by RSS by comparing the MW TPW
126 retrievals with those from ground-based Global Positioning System (gb-GPS) stations
127 (Mears et al, 2015; Wentz, 2015). Because the gb-GPS stations are nearly always located
128 on land, these validation studies use stations located on small and isolated islands (Mears
129 et al., 2015). RSS results for TPW collocated with those derived from gb-GPS over these
130 island stations show that their mean differences vary from station to station, and can be as
131 large as 2 mm. The mean difference also varies with surface wind speed, varying from 1
132 mm at low wind speeds to -1 mm at high wind (20 m/s) speeds. The difference is near zero
133 for the most common wind speeds (6 to 12 m/s). Because the uncertainty of the input
134 parameters and change of antenna for each GPS receiver (Bock et al., 2013), the mean
135 TPW(RSS) – TPW (gb-GPS) can vary from -1.5 mm to 1.5 mm for a single MW radiometer
136 (see Figure 4 in Mears et al., 2015). Wentz (2015) compared 17 years of Tropical Rainfall
137 Measuring Mission (TRMM) Microwave Imager (TMI) TPW collocated with gb-GPS
138 TPW over the region from 45°N to 45° S. The mean TMI- gb-GPS TPW bias was estimated
139 to be 0.45 mm with a standard deviation (σ) of 2.01 mm.

140 Unlike passive MW radiometers and infrared sensors, radio occultation (RO) is an
141 active remote sensing technique. RO can provide all-weather, high vertical resolution (from

142 ~100 m near the surface to ~1.5 km at 40 km) refractivity profiles (Anthes, 2011). The
143 basis of the RO measurement is a timing measured against reference clocks on the ground,
144 which are timed and calibrated by the atomic clocks at the National Institutes for Standards
145 and Technology (NIST). With a GPS receiver onboard the LEO (Low-Earth Orbiting)
146 satellite, this technique is able to detect the bending of radio signals emitted by GPS
147 satellites traversing the atmosphere. With the information about the relative motion of the
148 GPS and LEO satellites, the bending angle profile of the radio waves can be used to derive
149 all-weather refractivity, pressure, temperature, and water vapor profiles in the neutral
150 atmosphere (Anthes et al., 2008).

151 Launched in June 2006, COSMIC (Constellation Observing System for
152 Meteorology, Ionosphere, and Climate) RO data have been used to study atmospheric
153 temperature and refractivity trends in the lower stratosphere (Ho et al., 2009a, b, and 2012),
154 and modes of variability above, within, and below clouds (Biondi et al., 2012, 2013; Teng
155 et al., 2013; Scherllin-Pirscher et al., 2012; Zeng et al., 2012; Mears et al., 2012). Wick2008
156 demonstrated the feasibility of using COSMIC-derived TPW to validate SSM/I TPW
157 products over the east Pacific Ocean using one month of data. Many studies have
158 demonstrated the usefulness of RO derived water vapor to detect climate signals of El
159 Niño–Southern Oscillation (ENSO; Teng et al., 2013; Scherllin-Pirscher et al., 2012; Huang
160 et al., 2013), Madden-Julian Oscillation (MJO; Zeng et al., 2012), and improving moisture
161 analysis of atmospheric rivers (Neiman et al., 2008; Ma et al. 2011).

162 The objective of this study is to use COSMIC RO TPW to characterize the global
163 TPW values and trends derived from multiple MW radiometers over oceans, including
164 under cloudy and precipitating skies. COSMIC TPW from June 2006 to December 2013

165 are compared to co-located TPW derived from MW radiometers over the same time period.
166 Because RO data are not strongly sensitive to clouds and precipitation, COSMIC TPW
167 estimates can be used to identify possible MW TPW biases under different meteorological
168 conditions. We describe datasets and analysis method used in the comparisons in Section
169 2. The comparison results under clear skies and cloudy skies are summarized in Sections 3
170 and 4, respectively. The time series analysis is in Section 5. We conclude this study in
171 Section 6.

172

173 **2. RSS Version 7.0 Data and COSMIC TPW Data and Comparison Method**

174 **2.1 RSS Version 7.0 Data Ocean Products**

175 The RSS version 7.0 ocean products are available for SSM/I, SSMIS, AMSR-E,
176 WindSat, and TMI. The inversion algorithm is mainly based on Wentz and Spencer,
177 (1998), where above a cutoff in the liquid water column (2.45 mm), water vapor is no
178 longer retrieved. The various radiometers from the different satellites have been precisely
179 inter-calibrated at the radiance level by analyzing the measurements made by pairs of
180 satellites operating at the same time. This was done for the explicit purpose of producing
181 versions of the datasets that can be used to study decadal-scale changes in TPW, wind,
182 clouds, and precipitation, so special attention was focused on inter-annual variability in
183 instrument calibration. The calibration procedures and physical inversion algorithm used
184 to simultaneously retrieve TPW, surface wind speed (and thereby surface wind stress and
185 surface roughness) and the total liquid water content are summarized in Wentz (2013) and
186 Wentz (1997), respectively. This allows the algorithm to minimize the effect of wind speed,
187 clouds, and rain on the TPW measurement.

188 The RSS version 7.0 daily data are available on a 0.25° latitude x 0.25° longitude
189 grid for daytime and nighttime (i.e., 1440x720x2 daily per day). Figures 1a-d shows the
190 RSS V7.0 monthly mean F16 SSMIS TPW (in mm), surface skin temperature (in K), liquid
191 water path (LWP, in mm), and rain rate (RR, in mm/h), respectively, in 2007. Figure 1
192 shows that the variation and distribution of TPW over oceans (Figure 1a) is, in general,
193 closely linked to surface skin temperature variations over the Intertropical Convergence
194 Zone (ITCZ) (Figure 1b), which is modulated by clouds and the hydrological cycle (Soden
195 et al., 2002). The distribution of monthly TPW is consistent with that of cloud water, where
196 highest TPW values (and LWP and RR) occur in persistent cloudy and strong convective
197 regions over the tropical west Pacific Ocean near Indonesia.

198 Because COSMIC reprocessed TPW data are only available from June 2006 to
199 December 2013 (i.e., COSMIC2013), the SSM/I F15, SSMIS F16, SSMIS F17, together
200 with WindSat RSS Version 7.01 ocean products covering the same time period are used in
201 this study. Table 1 summarizes the starting date and end date for RSS SSM/I F15, SSMIS
202 F16, SSMIS F17, and WindSat data. The all sky daily RSS ocean products for F15, F16,
203 F17, and WindSat are downloaded from <http://www.remss.com/missions/ssmi>.

204

205 **2.2 COSMIC TPW Products**

206 The atmospheric refractivity N is a function of pressure P , temperature T , water
207 vapor pressure P_w , and water content W through the following relationship (Kursinski
208 1997; Zou et al. 2012):

209

$$210 \quad N = 77.6 \frac{P}{T} + 3.73 \times 10^5 \frac{P_w}{T^2} + 1.4W_{\text{water}} + 0.61W_{\text{ice}} \quad (1)$$

211

212 where P is the pressure in hPa, T is the temperature in K, P_w is the water vapor pressure in
213 hPa, W_{water} is the liquid water content in grams per cubic meter (gm^{-3}), and W_{ice} is the
214 ice water content in gm^{-3} . The last two terms generally contribute less than 1% to the
215 refractivity and may be ignored (Zou et al., 2012). However, they can be significant for
216 some applications under conditions of high cloud liquid or ice water content, as shown by
217 Lin et al. 2010; Yang and Zou 2012; Zou et al. 2012. We will neglect these terms in this
218 study, but because we are looking at small differences between MW and RO TPW in
219 cloudy and precipitating conditions in this paper, we estimate the possible contribution of
220 these terms to RO TPW and the consequences of neglecting them here. Since both of these
221 terms increase N , neglecting them in an atmosphere in which they are present will produce
222 a small positive bias in water vapor pressure P_w and therefore total precipitable water when
223 integrated throughout the entire depth of the atmosphere.

224 Typical value of cloud LWC range from $\sim 0.2 \text{ gm}^{-3}$ in stratiform clouds (Thompson,
225 2007) to 1 gm^{-3} in convective clouds (Thompson, 2007; Cober et al. 2001). Extreme values
226 may reach $\sim 2 \text{ gm}^{-3}$ in deep tropical convective clouds (i.e., cumulonimbus). Ice water
227 content values are smaller, typically $0.01 - 0.03 \text{ gm}^{-3}$ (Thompson, 2007). Heymsfield et al.,
228 (2002) reported high ice water content values ranging from $0.1 - 0.5 \text{ gm}^{-3}$ in tropical cirrus
229 and stratiform precipitating clouds, although it may rarely reach as high as 1.5 gm^{-3} in deep
230 tropical convective clouds (Leroy et al., 2017).

231 For extremely high values of W_{water} and W_{ice} of 2.0 and 0.5 gm^{-3} , the contributions
232 to N are 2.8 and 0.3 respectively. The values of N in the atmosphere decrease exponentially
233 upward, from ~ 300 near the surface to ~ 150 at $P=500$ hPa. Using the above extreme values

234 at 500 hPa, W_{water} may contribute from up to 1.6% of N and W_{ice} up to 0.2%. Thus we may
235 assume that in most cases the error in N due to neglecting these terms will be less than 1%.
236 The effect on TPW will be even less, since clouds do not generally extend through the full
237 depth of the atmosphere. Finally, the ~ 200 km horizontal averaging scale of the RO
238 observation footprint makes it unlikely that such extremely high values of water and ice
239 content will be present over this scale. We conclude that the small positive bias in RO TPW
240 introduced by neglecting the liquid and water terms in (1) will be less than 1%.

241 To resolve the ambiguity of COSMIC refractivity associated with both temperature
242 and water vapor in the lower troposphere, a 1D-var algorithm ([http://cosmic-
243 io.cosmic.ucar.edu/cdaac/doc/documents/1dvar.pdf](http://cosmic-io.cosmic.ucar.edu/cdaac/doc/documents/1dvar.pdf)) is used to derive optimal temperature
244 and water vapor profiles while temperatures and water vapor profiles from the ERA-
245 Interim reanalysis are used as a priori estimates (Neiman et al. 2008; Zeng et al. 2012).

246 Note that because RO refractivity is very sensitive to water vapor variations in the
247 troposphere (Ho et al. 2007), and is less sensitive to temperature errors, RO-derived water
248 vapor product is of high accuracy (Ho et al. 2010 a, b). It is estimated that 1K of
249 temperature error will introduce less than 0.25 g/kg of water vapor bias in the troposphere
250 in the 1D-var retrievals. Although the first guess temperature and moisture are needed for
251 the 1D-Var algorithm, the retrieved water vapor profiles are weakly dependent on the first
252 guess water vapor profiles (Neiman et al. 2008).

253 The horizontal footprint of a COSMIC observation is about 200 km in the lower
254 troposphere and its vertical resolution is about 100 m near the surface and 1.5 km at 40 km.
255 The COSMIC post-processed water vapor profiles version 2010.2640 collected from
256 COSMIC Data Analysis and Archive Center (CDAAC)

257 (<http://cosmicio.cosmic.ucar.edu/cdaac/index.html>) are used to construct the COSMIC
258 TPW data. To further validate the accuracy of COSMIC-derived water vapor, we have
259 compared COSMIC TPW with those derived from ground-based GPS (i.e., International
260 Global Navigation Satellite Systems–IGS, Wang et al. 2007) which are assumed to be
261 independent of location. Only those COSMIC profiles whose lowest penetration heights
262 are within 200 meters of the height of ground-based GPS stations are included. Results
263 showed that the mean global difference between IGS and COSMIC TPW is about -0.2 mm
264 with a standard deviation of 2.7 mm (Ho et al., 2010a). Similar comparisons were found
265 by Teng et al. (2013) and Huang et al. (2013).

266

267 **2.3 Preparation of COSMIC TPW data for Comparison**

268 In this study, only those COSMIC water vapor profiles penetrating lower than 0.1
269 km are integrated to compute TPW. Approximately 70% to 90% of COSMIC profiles
270 reach to within 1 km of the surface (Anthes et al., 2008). Usually more than 30% of
271 COSMIC water vapor profiles reach below 0.1 km in the mid-latitudes and higher latitudes,
272 and a little bit less than 10% in the tropical regions. To compensate for the water vapor
273 amount below the penetration height, we follow the following procedure:

- 274 i) we assume the relative humidity below the penetration height is equal to 80%. This is
275 a good assumption especially over oceans near the sea surface (Mears et al., 2015);
- 276 ii) the temperatures below the penetration height are taken from the ERA-interim
277 reanalysis;
- 278 iii) we compute the water vapor mixing ratio below the penetration heights;

279 iv) we integrate the TPW using COSMIC water vapor profiles above the penetration
280 heights with those water vapor profile below the penetration heights.

281 The COSMIC TPW estimates are not very sensitive to the assumption of 80% relative
282 humidity below 0.1 km (Step i above). The assumption of 80% +/-10% (i.e., 90% and 70%)
283 relative humidity below 0.1 km introduces an uncertainty of about +/- 0.03 mm in the WV
284 – COSMIC comparisons for all conditions. As shown in Section 4, this uncertainty is small
285 compared to the observed differences between the RO and MW estimates.

286 Pairs of MW and RO TPW estimates collocated within 50 km and one hour are
287 collected. The location of RO observation is defined by the RO tangent point at 4-5 km
288 altitude. Wick2008 used MW-RO pairs within 25 km and one hour in time. To evaluate
289 the effect of the spatial difference on the TPW difference, we also computed TPW
290 differences for MW-RO pairs within 75 km, 100 km, and 150 km, and 200 km. We found
291 the larger spatial difference increases the mean TPW biases slightly to +/- 0.25 mm and the
292 standard deviations to +/- 1.91 mm, which is likely because of the high spatial variability
293 of water vapor. Note that, although not shown, the mean biases and standard deviations of
294 the mean biases are slightly larger over the tropics than over mid-latitudes. This could be
295 because of the combined effect of the larger spatial TPW variation in the tropical region
296 than those in the mid-latitudes (see Fig. 1a, and Neiman et al., 2008; Teng et al., 2013;
297 Mears et al., 2015) and the fact that the MW TPW retrieval uncertainty is also larger over
298 stronger convection regions. More results are detailed in Section 4.

299 With a $0.25^{\circ} \times 0.25^{\circ}$ grid, there are about 20 to 60 MW pixels matching one
300 COSMIC observation. The number of pixels varies at different latitudes. A clear MW-RO
301 pair is defined as instances when *all* the TCW values for the collocated MW pixels are

302 equal to zero. A cloudy MW-RO ensemble is defined as instances when *all* the TCW values
303 from the collocated MW pixels are larger than zero. Partly cloudy conditions (some of
304 pixels zero and some non-zero) are excluded from this study. The cloudy ensembles are
305 further divided into precipitating and non-precipitating conditions. MW-RO pairs are
306 defined as cloudy non-precipitating when less than 20% of MW pixels have rainfall rates
307 larger than zero mm/hour. Cloudy precipitating MW-RO pairs are defined when more than
308 20% of the pixels have rainfall rates larger than zero. Because microwave radiances are not
309 sensitive to ice, we treat cloudy pixels of low density like cirrus clouds as clear pixels.

310 The matching pairs of RO and MW observations are not distributed uniformly over
311 the world oceans. In fact, they are heavily concentrated in middle latitudes, as shown in
312 Figure 1e. This biased distribution is caused by several factors, including the polar orbits
313 of the satellites, which produce more observations in higher latitudes, and also the failure
314 of many COSMIC RO soundings to penetrate to 0.1km in the subtropics and tropics (due
315 to super-refraction which is often present in these regions). Thus the results presented here,
316 especially the trends, are not representative of global averages. However, the main purpose
317 of this paper is to compare two independent satellite systems for obtaining TPW under
318 varying sky conditions. If the agreement is good, one has confidence in both systems. In
319 this case, SSM/I and WindSat estimates of TPW will be verified and then can be used with
320 confidence globally, including where RO observations are sparse or do not exist.

321

322 **3. Comparison of MW and RO TPW with clear skies**

323 In total there are 26,678 F15-RO pairs, 32,610 F16-RO pairs, 31,291 F17-RO pairs,
324 and 21,996 WindSat-RO pairs from June 2006 to December 2013, respectively. Figures

325 2a-d show scatter plots for F15-COSMIC TPW, F16-COSMIC TPW, F17-COSMIC TPW,
326 and WindSat-COSMIC TPW under clear skies. Figures 2a-d show that the MW clear sky
327 TPW from F15, F16, F17, and WindSat are all very consistent with those from co-located
328 COSMIC observations. As summarized in Table 2, under clear conditions where SSM/I
329 provides high quality TPW estimates, the mean TPW bias between F16 and COSMIC
330 (F16- COSMIC) is equal to 0.03 mm with a standard deviation σ of 1.47 mm. The mean
331 TPW differences are equal to 0.06 mm with a σ of 1.65 mm for F15, 0.07 mm with a σ of
332 1.47 mm for F17, and 0.18 mm with a σ of 1.35 mm for WindSat. The reason for larger
333 standard deviation for F15 may be because the F15 data after August 2006 were corrupted
334 by the “rad-cal” beacon that was turned on at this time (Hilburn and Wentz, 2008). On 14
335 August 2006, a radar calibration beacon (RAD-CAL) was activated on F15. This radar
336 interfered with the SSM/I, primarily the 22V channel, which is a key channel for water
337 vapor retrievals. Although a correction method derived by Hilburn and Wentz (2008) and
338 Hilburn (2009) was applied, the 22 V channel is not being full corrected (Wentz, 2012).
339 As a result, there are still errors in the water vapor retrievals. F16 had solar radiation
340 intrusion into the hot load during the time period, while F17 and WindSat had no serious
341 issues.

342

343 **4. Global comparisons of MW and RO TPW with cloudy skies**

344 **4.1 Comparison of MW, RO, and Ground-based GPS TPW**

345 Figures 3a-c depict the scatter plots for F16-COSMIC pairs under cloudy, cloudy
346 non-precipitating, and precipitating conditions from June 2006 to December 2013 over
347 oceans. While there is a very small bias (0.031 mm) for clear pixels (Figure 2b), there is a

348 significant positive TPW bias (0.794 mm) under cloudy conditions (Figure 3a). This may
349 explain the close to 0.45 mm mean TMI-gb GPS TPW biases found by Wentz et al., (2015)
350 where a close to 7 years of data were used. Figure 3c depicts that the large SSM/I TPW
351 biases under cloudy skies are mainly from the pixels with precipitation (mean bias is equal
352 to 1.825 mm) although precipitation pixels are of about less than 6% of the total F16-
353 COSMIC pairs. Because RO measurements are not significantly affected by clouds and
354 precipitation, the biases mainly result from MW retrieval uncertainty under cloudy
355 conditions. The fact that the MW-COSMIC biases for precipitating conditions (1.825 mm,
356 Figure 3c and 1.64-1.88 mm in Table 2) is much larger than those for cloudy, but non-
357 precipitating conditions, indicates that significant scattering and absorbing effects are
358 present in the passive MW measurements when it rains. The correlation coefficients for
359 F15-RO, F16-RO, F17-RO, and WindSat-RO pairs for all sky conditions are all larger than
360 0.96 (not shown).

361 MW and gb-GPS TPW comparisons show similar differences as the MW-RO
362 differences under different sky conditions. We compared F16 pixels with those from gb-
363 GPS within 50 km and 1 hour over the 33 stations studied by Mears et al. (2015) from 2002
364 to 2013. Figures 4a-d depict the scatter plots for F16-gb-GPS TPW under clear, cloudy,
365 cloudy non-precipitating, and cloudy precipitating conditions, respectively. The F16-gb-
366 GPS mean biases are equal to 0.241 mm (clear skies), 0.614 mm (cloudy skies), 0.543 mm
367 (cloudy-non precipitation) and 1.197 mm (precipitation), which are similar to those
368 estimated from MW-RO comparisons (Table 2).

369 The above results show that the MW estimates of TPW are biased positively
370 compared to both the RO and the ground-based GPS estimates, which are independent

371 measurements. The biases are smallest for clear skies and largest for precipitating
372 conditions, with cloudy, non-precipitating biases in between. Overall, the results suggest
373 that clouds and especially precipitation contaminate the MW radiometer measurements,
374 which in turn affect the MW TPW retrievals.

375

376 **4.2 Time Series of MW, RO, and Ground-based TPW Biases under Various** 377 **Meteorological Conditions**

378 To further examine how rain and cloud droplets affect the MW TPW retrievals, we
379 show how the F16-RO TPW biases vary under different meteorological conditions in
380 Figure 5. The bias dependence on wind speed (Figure 5a) is small. Unlike the results from
381 Mears et al., (2015), the mean TPW biases between F16 and COSMIC are within 0.5 mm
382 with high winds (wind speed larger than 20 m/s). Figure 5b indicates that the F16-COSMIC
383 bias is larger with TPW greater than about 10 mm, which usually occurs under cloudy
384 conditions. The F16-COSMIC biases can be as large as 2.0 mm when the rainfall rate is
385 larger than 1 mm/hour (Figure 5c), which usually occurs with high total liquid cloud water
386 conditions. The F16 TPW biases can be as large as 2 mm when total cloud water is larger
387 than 0.3 mm (Figure 5d). Figure 5e shows that the larger F16-COSMIC TPW biases (2-3
388 mm) mainly occur over regions with surface skin temperature less than 270 K (higher
389 latitudes, see Figure 1b). The F15, F17, and WindSat TPW biases under different
390 meteorological conditions are very similar to those of F16 (not shown).

391 In Figure 6 we compare RSS V7.0 F16 MW TPW to the ground-based GPS TPW
392 over various meteorological conditions. The magnitudes of the MW-gb-GPS TPW
393 differences under high rain rate and high total cloud water conditions are somewhat smaller

394 than those of MW-RO pairs (varying from about 0.5 mm to 2.0 mm), which may be because
395 most of the MW-gb-GPS samples are collected under low rain rates (less than 1 mm/hour)
396 conditions.

397

398 **5. Eight Year Time Series and Trend Analysis under All Skies**

399 **5.1 Monthly Mean TPW Time Series Comparison**

400 To further examine MW TPW long-term stability and trend uncertainty due to rain
401 and water droplets for different instruments, we compared time series of the MW and
402 COSMIC monthly mean TPW differences from June 2006 to December 2013. Figures 7a-
403 d show the monthly mean F16-COSMIC TPW differences from June 2006 to December
404 2013 for clear, cloudy, cloudy non-precipitating, and precipitating conditions. In general,
405 the microwave TPW biases under different atmospheric conditions are positive and stable
406 from June 2006 to December 2013, as reflected in relatively small standard deviation
407 values (Table 3). Except for F15, the standard deviations of the monthly mean TPW
408 anomaly range are less than 0.38 mm (Table 3). In contrast, the F15-COSMIC monthly
409 mean σ range from 0.48 mm to 0.69 mm with different conditions.

410 Table 3 also shows the trend in the RO estimates of TPW differences over the eight-
411 year period of study. The trends are range from -0.12 mm/decade (WindSat, clear skies) to
412 2.52 mm/decade (F15, precipitating conditions). The overall trend of TPW as estimated by
413 RO (second line in each row of Table 3) is positive as discussed in the next section. Table
414 3 shows that in general the trends are more strongly positive under cloudy and precipitating
415 conditions compared to clear conditions.

416

417 **5.2 De-seasonalized Trends of MW-RO Differences and TPW**

418 Figure 8 depicts the de-seasonalized trends of the MW-RO TPW differences for
419 F15 (Figure 8a), F16 (Figure 8b), F17 (Figure 8c), and WindSat (Figure 8d) under cloudy
420 skies. Except for F15, the de-seasonalized trends of the MW-RO TPW differences for the
421 MW radiometers are close to zero, indicating little change over these eight years. The
422 trends of the biases associated with F15, F16, F17 and WindSat under all sky conditions
423 range from -0.09 to 0.27 mm/decade (details not shown).

424 The reason for larger standard deviations of the MW minus RO differences for F15
425 (Tables 2 and 3 and Figure 8a) is very likely because the F15 data after August 2006 were
426 corrupted by the “rad-cal” beacon that was turned on at this time. Adjustments were derived
427 and applied to reduce the effects of the beacon, but the final results still show excess noise
428 relative to uncorrupted measurements (Hilburn and Wentz, 2008). RSS does not
429 recommend using these measurements for studies of long-term change. Thus we consider
430 the F15 data less reliable during the period of our study.

431 Figure 9 shows the de-seasonalized time series of the monthly mean TPW for all
432 MW and RO pairs under all sky conditions. The close to eight year trends for TPW
433 estimated from both passive MW radiometers and active COSMIC RO sensors are positive
434 and very similar in magnitude. The mean trend of all COSMIC RO TPW is 1.79
435 mm/decade with a 95% confidence interval of (0.96, 2.63) mm/decade while the mean
436 trend from all the MW estimates is 1.78 mm/decade with a 95% confidence interval of
437 (0.94, 2.62). This close agreement between completely independent measurements lends
438 credence to both estimates. The mean TPW over this period, calculated from all MW data

439 in our data set was 26.04 mm; thus the trend of 1.78 mm/decade represents a trend of
440 approximately 6.9% per decade for our data set.

441 As discussed earlier, the trend of 1.78 mm/decade is heavily biased toward middle
442 latitudes (40°N-60°N and 40°-65°S) and is not representative of a global average. In fact,
443 it is four to six times larger than previous estimates over earlier time periods. For example,
444 Durre et al. (2009) estimated a trend of 0.45 mm/decade for the Northern Hemisphere over
445 the period 1973-2006. Trenberth et al. (2005) estimated a global trend of 0.40 +/- 0.09
446 mm/decade for the period 1988 to 2001. Using SSM/I data, Wentz et al. (2007) estimated
447 and an increase of 0.354 mm/decade over the period 1997-2006. The 100-year trend in
448 global climate models is variable, ranging from 0.55 to 0.72 mm/decade (Roman et al.,
449 2014).

450 The very close agreement between RO and MW observations where they co-exist
451 gives credibility to both observing systems and allows us to use global MW data to compute
452 global TPW trends over all oceanic regions, including where RO observations are sparse
453 or absent. Figure 10 shows the global map of TPW trends over oceans using all F16, F17,
454 and WindSat data from 2006 to 2013. Figure 10 shows that the positive trends in TPW
455 occur mainly over the central and north Pacific, south of China and west of Australia,
456 south-east of South America, and east of America. Positive trends also exist in general
457 over the middle latitudes (40°N-60°N and 40°-65°S) where most of our matching RO and
458 MW data pairs occur.

459 Mears et al. (2017) computed global average (60°S to 60°N) TPW using a number
460 of data sets from 1979 to 2014. Figure 11 shows the data from the ERA-Interim reanalysis
461 (Dee et al. 2011), RSS MW, and COSMIC. (This figure was obtained using the same data

462 used to construct Figure 2.16 in Mears et al., 2017). Fig. 11 shows close agreement between
463 RSS MW and COSMIC. The global mean trend from June 2006 to December 2013 from
464 the COSMIC observations is 0.32 mm/decade and for RSS MW it is 0.31 mm/decade.

465

466 **6. Conclusions and Discussions**

467 RSS water vapor products have been widely used for climate research. The newly
468 available RSS V7.0 data products have been processed using consistent calibration
469 procedures (Wentz, 2013). This was done for the explicit purpose of producing versions of
470 the datasets that can be used to study decadal scale changes in TPW, wind, clouds, and
471 precipitation. These water vapor products are mainly verified by comparing to either
472 reanalyses, radiosondes measurements, or other satellite data. However, because the
473 quality of these datasets may also vary under different atmospheric conditions, the
474 uncertainty in long-term water vapor estimates may still be large. In this study, we used
475 TPW estimates derived from COSMIC active RO sensors to identify TPW uncertainties
476 from four different MW radiometers under clear, cloudy, cloudy/non-precipitating, and
477 cloudy/precipitating skies over nearly eight years (from June 2006 to December 2013).
478 Because RO data have low sensitivity to clouds and precipitation, RO-derived water vapor
479 products are useful to identify the possible TPW biases retrieved from measurements of
480 passive microwave imagers under different sky conditions. We reach the following
481 conclusions:

482 1) Clear sky biases: The collocated COSMIC RO TPW estimates under clear skies
483 are highly consistent with the MW TPW estimates under clear sky conditions (within +/-
484 0.2 mm and with a correlation coefficient greater than 0.96). The mean TPW bias between

485 F16 and COSMIC (F16- COSMIC) is equal to 0.03 mm with a standard deviation σ of 1.47
486 mm. The mean TPW differences are equal to 0.06 mm with a σ of 1.65 mm for F15, 0.07
487 mm with a σ of 1.47 mm for F17, and 0.18 mm with a σ of 1.35 mm for WindSat. The
488 consistent F15-COSMIC, F16-COSMIC, F17-COSMIC, and WindSat-COSMIC TPW
489 under clear skies show that COSMIC TPW can be used as reliable reference data to identify
490 and correct TPW among different MW imagers for other sky conditions.

491 2) Biases under cloudy skies: While there are very small biases for clear pixels,
492 there are significant positive MW TPW biases (~ 0.80 mm) under cloudy conditions when
493 compared to RO TPW. The large SSM/I TPW biases under cloudy skies result mainly from
494 the pixels with precipitation. The mean bias is equal to 1.83 mm for COSMIC-F16 pairs,
495 which is much larger than the bias for cloudy, but non-precipitating conditions. This
496 indicates that the significant scattering and absorbing effects are present in the passive MW
497 measurements when it rains. The F16 – Ground-based GPS mean biases are equal to 0.24
498 mm (for clear skies), 0.61 mm (for cloudy skies), 0.54 mm (for cloudy/non-precipitating
499 skies) and 1.2 mm (for precipitating skies) which are consistent with those from F16-
500 COSMIC comparisons.

501 3) Biases among different instruments: Using RO TPW estimates collocated with
502 different MW instruments, we are able to identify possible TPW inconsistencies among
503 MW instruments even they are not collocated. The de-seasonalized trends in MW-RO TPW
504 differences for three MW radiometers (i.e., F16, F17, and WindSat) are close to zero,
505 indicating consistency among these radiometers. However, the F15-COSMIC differences
506 are larger and show a significant trend over the eight years of the study. It is likely that F15

507 data after August 2006 were corrupted by the “rad-cal” beacon that was turned on at this
508 time.

509 4) Trend of TPW under all skies: The eight-year trends of TPW estimated from
510 both passive MW radiometer and active COSMIC sensors in our data set show increasing
511 TPW, with slightly higher trends under cloudy conditions. The mean trend of COSMIC
512 RO TPW collocated with MW observations in our data set is 1.79 mm/decade with a 95%
513 confidence interval of (0.96, 2.63) mm/decade. The corresponding mean trend from all the
514 MW estimates is 1.78 mm/decade with a 95% confidence interval of (0.94, 2.62). The mean
515 trend from all the MW estimates under cloudy conditions is 1.93 mm/decade with a 95%
516 confidence interval of (0.97, 2.89). The mean trend from all the COSMIC RO TPW
517 estimates under cloudy conditions is 1.82 mm/decade with a 95% confidence interval of
518 (0.88, 2.76). These increases represent about a 6.9% per decade increase in the mean TPW
519 of our data set. The close agreement between completely independent measurements lends
520 credence to both estimates.

521 The trends of TPW in our data set, which are heavily biased toward middle latitudes
522 (40°N-60°N and 40°S-65°S) are higher than previous global estimates over earlier time
523 periods by about a factor of four to six. As also shown by the regional distribution of TPW
524 trends estimated from the MW observations, the large positive trends in these latitudes,
525 which are the main latitudes of extratropical storm tracks, are a strong confirmation of the
526 water vapor-temperature feedback in a warming global atmosphere particularly under
527 cloudy conditions.

528 Other studies have suggested that this positive feedback results in a nearly constant
529 global mean relative humidity (Soden and Held, 2006; Sherwood et al., 2010). However,

530 it is difficult to directly relate our estimated TPW trends to constant RH hypothesis of
531 Earth's atmosphere under global warming. The global mean surface temperature has been
532 rising at about the rate of 0.2 K/decade in the past twenty years. A 0.2K increase in
533 temperature would produce about a 1.4% increase in saturation water vapor pressure based
534 on the Clausius-Clapeyron equation. To maintain a constant RH for this temperature
535 increase, the actual water vapor pressure (and specific humidity) would also have to
536 increase by 1.4%. In this study, we observe an increase of TPW in our dataset of about 1.78
537 mm/decade which is 6.9 percent increase per decade in TPW. Our dataset is dominated
538 mainly by cloudy samples over middle latitudes (40°N-60°N and 40°-65°S). Thus, from
539 these numbers alone we would expect an increase in mean RH under cloudy conditions by
540 more than 6%, which is unlikely and well outside the range of changes in relative humidity
541 in models (e.g. Figure 2 in Sherwood et al., 2010). However, the changes in the global
542 mean RH are not related in such a simple fashion to changes in the global mean temperature
543 and precipitable water. For example, Figure 10 depicts that there are very large differences
544 in the spatial distribution of TPW changes, which shows regional variations of +/- 4
545 mm/decade. Thus, some regions are drying and others are moistening. The variations in
546 global mean surface temperature are also large, but very different from those of TPW, with
547 the polar regions and continents warming up much faster than the atmosphere over the
548 oceans. In cold polar regions, an increase in temperature will result in a smaller increase in
549 saturation vapor pressure than the same increase in temperature in the tropics. The global
550 evaporation and precipitation patterns also vary greatly, as water vapor transport is
551 important in the global water vapor balance. All of this, as discussed by Held and Soden
552 (2000), Soden and Held (2006), and Sherwood et al. (2010) means that the relationships

553 between global mean temperature increase, TPW changes, and the resulting change in
554 global mean RH are not simple.

555

556 **Acknowledgements.** This work is supported by the NSF CAS AGS-1033112. We thank
557 Eric DeWeaver (NSF) and Jack Kaye (NASA) for sponsoring this work.

558

559

560

561

562

563

564

565

566

567

568

569

570

571

572

573

574

575

576 **References**

- 577 Anthes, R. A., P. Bernhardt, Y. Chen, L. Cucurull, K. Dymond, D. Ector, S. Healy, S.-P.
578 Ho, D. Hunt, Y.-H. Kuo, H. Liu, K. Manning, C. McCormick, T. Meehan, W. Randel,
579 C. R. Rocken, W. Schreiner, S. Sokolovskiy, S. Syndergaard, D. Thompson, K.
580 Trenberth, T.-K. Wee, Z. Zeng, 2008: The COSMIC/FORMOSAT-3 Mission: Early
581 Results, *Bul. Amer. Meteor. Sci.* 89, No.3, 313-333, DOI: 10.1175/BAMS-89-3-313.
- 582 Anthes, R.A., 2011: Exploring Earth's atmosphere with radio occultation: contributions to
583 weather, climate and space weather. *Atmos. Meas. Tech.*, 4, 1077-1103,
584 DOI:10.5194/amt-4-1077-2001.
- 585 Biondi, R., W. Randel, S.-P. Ho, T. Neubert, and S. Syndergaard, 2012: Thermal
586 structure of intense convective clouds derived from GPS radio occultations. *Atmos.*
587 *Chem. Phys.*, doi:10.5194/acp-12-5309-2012.
- 588 Biondi, R., S.-P. Ho, W. Randel, T. Neubert and S. Syndergaard, 2013: Tropical cyclone
589 cloud-top heights and vertical temperature structure detection using GPS radio
590 occultation measurements, *J. Geophys. Research*, VOL. 118, 1–13,
591 doi:10.1002/jgrd.50448.
- 592 Bock, O., Bossler, P., Bourcy, T., David, L., Goutail, F., Hoareau, C., Keckhut, P.,
593 Legain, D., Pazmino, A., Pelon, J., Pipis, K., Poujol, G., Sarkissian, A., Thom, C.,
594 Tournois, G., and Tzanos, D. 2013: Accuracy assessment of water vapour
595 measurements from in situ and remote sensing techniques during the DEMEVAP
596 2011 campaign at OHP, *Atmos. Meas. Tech.*, 6, 2777–2802, doi:10.5194/amt-6-
597 2777-2013.
- 598 Cober, S. G., G. A. Isaac, and J. W. Strapp, 2001: Characterizations of aircraft icing

599 environments that include supercooled large drops. *J. Appl. Meteor.*, 40, 1984–2002.

600 Durre, I., C. N. Williams Jr., X. Yin, and R. S. Vose, 2009: Radiosonde-based trends in
601 precipitable water over the Northern Hemisphere: An update, *J. Geophys. Res.*, 114,
602 D05112, doi:10.1029/2008JD010989.

603 Dee D.P., S.M. Uppala, A.J. Simmons, P. Berrisford, P. Poli, S. Kobayashi, U. Andrae,
604 M.A. Balmaseda, G. Balsamo, P. Bauer, P. Bechtold, A.C.M. Beljaars, L. van de
605 Berg, J. Bidlot, N. Bormann, C. Delsol, R. Dragani, M. Fuentes, A.J. Geer, L.
606 Haimberger, S.B. Healy, H. Hersbach, E.V. Hólm, L. Isaksen, P. Kållberg, M.
607 Köhler, M. Matricardi, A.P. McNally, B.M. Monge-Sanz, J.-J. Morcrette, B.-K.
608 Park, C. Peubey, P. de Rosnay, C. Tavalato, J.-N. Thepaut, and F. Vitart, 2011: The
609 ERA-Interim reanalysis: configuration and performance of the data assimilation
610 system. *Q. J. R. Meteorol. Soc.* **137**: 553–597. DOI:10.1002/qj.828

611 Elsaesser, G. S. and C. D. Kummerow, 2008: Towards a fully parametric retrieval of the
612 non-raining parameters over the global ocean. *J. Appl. Meteor. & Climatol.*, 47, 1590
613 – 1598.

614 Fetzer, E. J., B. H. Lambriksen, A. Eldering, H. H. Aumann, and M.T. Chahine, M.T.,
615 2006: Biases in total precipitable water vapor climatologies from atmospheric infrared
616 sounder and advanced microwave scanning radiometer. *J. Geophys. Res.*, 111,
617 D09S16, doi: 10.1029/2005JD006598.

618 Fetzer, E. J., W.G. Read, D. Waliser, B. H. Kahn, B. Tian, H. Vömel, F. W. Irion, H. Su,
619 A. Eldering, M. T. Juarez, J. Jiang, and V. Dang, 2008: Comparison of upper
620 tropospheric water vapor observations from the Microwave Limb Sounder and
621 Atmospheric Infrared Sounder. *J. Geophys. Res.*, 113/D22, D22110.

622 Held, I. M., and B. J. Soden, 2000: Water vapor feedback and global warming, *Annu. Rev.*
623 *Energy Environ.*, 25, 441–475, doi:10.1146/annurev.energy.25.1.441.

624 Heymsfield, A. J., A. Bansemer, P. R. Field, S. L. Durden, J. L. Stith, J. E. Dye, W. Hall,
625 and C. A. Grainger, 2002: Observations and parameterizations of particle size
626 distributions in deep tropical cirrus and stratiform precipitating clouds: Results from in
627 situ observations in TRMM field campaigns. *J. Atmos. Sci.*, 59, 3457–3491,
628 doi:10.1175/1520-0469(2002)059, 3457.

629 Hilburn, K.A., 2009: Including temperature effects in the F15 RADCAL Beacon
630 correction. RSS Technical Report 051209, Remote Sensing Systems, Santa Rosa, CA.
631 http://www.remss.com/papers/RSS_TR051209_RADCAL.pdf.

632 Hilburn, K. A., F. J. Wentz, 2008: Mitigating the impact of RADCAL beacon
633 contamination on F15 SSM/I ocean retrievals, *Geophysical Research Letters*, 35,
634 L18806, doi:10.1029/2008GL034914.

635 Ho, S.-P., Kuo, Y.-H., and Sokolovskiy, S., 2007: Improvement of the temperature and
636 moisture retrievals in the lower troposphere using AIRS and GPS radio occultation
637 measurements. *J. Atmos. Oceanic Technol.*, 24, 1726-1739,
638 doi:10.1175/JTECH2071.1.

639 Ho, S.-P., G. Kirchengast, S. Leroy, J. Wickert, A. J. Mannucci, A. K. Steiner, D. Hunt,
640 W. Schreiner, S. Sokolovskiy, C. O. Ao, M. Borsche, A. von Engel, n,
641 U. Foelsche, S. Heise, B. Iijima, Y.-H. Kuo, R. Kursinski, B. Pirscher, M. Ringer, C.
642 Rocken, and T. Schmidt, 2009a: Estimating the Uncertainty of using GPS Radio
643 Occultation Data for Climate Monitoring: Inter-comparison of CHAMP Refractivity
644 Climate Records 2002-2006 from Different Data Centers, *J. Geophys.*

645 *Res.*, doi:10.1029/2009JD011969.

646 Ho, S.-P., M. Goldberg, Y.-H. Kuo, C.-Z. Zou, W. Schreiner, 2009b: Calibration of
647 Temperature in the Lower Stratosphere from Microwave Measurements using
648 COSMIC Radio Occultation Data: Preliminary Results, *Terr. Atmos. Oceanic Sci.*,
649 Vol. 20, doi: 10.3319/TAO.2007.12.06.01(F3C).

650 Ho, S.-P., Y.-H. Kuo, W. Schreiner, X. Zhou, 2010a: Using SI-traceable Global Positioning
651 System Radio Occultation Measurements for Climate Monitoring [In “States of the
652 Climate in 2009]. *Bul. Amer. Meteor. Sci.*, 91 (7), S36-S37.

653 Ho, S.-P., Zhou X., Kuo Y.-H., Hunt D., Wang J.-H., 2010b: Global Evaluation of
654 Radiosonde Water Vapor Systematic Biases using GPS Radio Occultation from
655 COSMIC and ECMWF Analysis. *Remote Sensing*. 2010; 2(5):1320-1330.

656 Ho, S.-P., D. Hunt, A. K. Steiner, A. J. Mannucci, G. Kirchengast, H. Gleisner, S. Heise,
657 A. von Engel, C. Marquardt, S. Sokolovskiy, W. Schreiner, B. Scherllin-Pirscher,
658 C. Ao, J. Wickert, S. Syndergaard, K. B. Lauritsen, S. Leroy, E. R. Kursinski, Y.-H.
659 Kuo, U. Foelsche, T. Schmidt, and M. Gorbunov, 2012: Reproducibility of GPS
660 Radio Occultation Data for Climate Monitoring: Profile-to-Profile Inter-comparison
661 of CHAMP Climate Records 2002 to 2008 from Six Data Centers, *J. Geophys.*
662 *Research*. VOL. 117, D18111, doi:10.1029/2012JD017665.

663 Huang, C.-Y., W.-H. Teng, S.-P. Ho, Y.-H. Kuo, 2013: Global Variation of COSMIC
664 Precipitable Water over Land: Comparisons with Ground-based GPS Measurements
665 and NCEP Reanalyses, *Geophysical Research Letters*, DOI: 10.1002/grl.50885.

666 IPCC, 2013: Climate Change 2013: The Physical Science Basis. Contribution of Working
667 Group I to the Fifth Assessment Report of the Intergovernmental Panel on Climate

668 Change (IPCC). Cambridge University Press, Cambridge, United Kingdom and New
669 York, NY, USA, 1535 pp, doi:10.1017/CBO9781107415324.

670 John, V. O. and B.J. Soden, 2007: Temperature and humidity biases in global climate
671 models and their impacts on climate feedbacks. *Geophysical Research Letters*, 34,
672 L18605, doi:10.1029/2007GL030736.

673 Knuteson, R., S. Bedka, J. Roman, D. Tobin, D. Turner, and H. Revercomb, 2010: AIRS
674 and IASI Precipitable Water Vapor (PWV) Absolute Accuracy at Tropical, Mid-
675 Latitude, and Arctic Ground-Truth Sites. Presented at the International TOVS Study
676 Conference, Monterey, CA, USA, 14-10 April 2010, available online at
677 <http://cimss.ssec.wisc.edu/itwg/itsc/itsc17/>.

678 Kursinski, E.R., G.A. Hajj, J.T. Schofield and R.P. Linfield, 1997: Observing Earth's
679 atmosphere with radio occultation measurements using the Global Positioning
680 System. *J. Geophys. Res.* 102, No. D19, 23,429-23,465.

681 Larar, A. M., W. L. Smith, D. K. Zhou, X. Liu, H. Revercomb, J. P. Taylor, S. M. Newman,
682 and P. Schlüssel, 2010: IASI spectral radiance validation inter-comparisons: case study
683 assessment from the JAIVEx field campaign, *Atmos. Chem. Phys.*, 10, 411-430.

684 Leroy, D., Fontaine, E., Schwarzenboeck, A., Strapp, J. W., Korolev, A., McFarquhar, G.,
685 Dupuy, R., Gourbeyre, C., Lilie, L., Protat, A., Delanoë, J., Dezitter, F., and Grandin,
686 A., 2017: Ice crystal sizes in high ice water content clouds. Part 2: Statistics of mass
687 diameter percentiles in tropical convection observed during the HAIC/HIWC project,
688 *J. Atmos. Oceanic Technol.*, doi: 10.1175/JTECH-D-15-0246.1.

689 Lin, L., X. Zou, R. Anthes, and Y.-H. Kuo, 2010: COSMIC GPS cloudy profiles. *Mon.*
690 *Wea. Rev.*, 138, 1104–1118.

691 Luers, J. K. and R.E. Eskridge, 1998: Use of radiosonde temperature data in climate
692 studies. *J. of Climate*, 11, 1002–1019.

693 Ma, Z., Y.-H. Kuo, F. M. Ralph, P. J. Neiman, G. A. Wick, E. Sukovich, and B. Wang,
694 2011: Assimilation of GPS radio occultation data for an intense atmospheric river
695 with the NCEP regional GSI system. *Mon. Wea. Rev.*, 139, 2170–2183,
696 doi:10.1175/2011MWR3342.1.

697 Mears, C., J. Wang, S.-P. Ho, L. Zhang, and X. Zhou, 2012: Global Climate Hydrological
698 cycle, Total column water vapor [in “State of the Climate in 2011”]. *Bull. Amer.*
699 *Meteor. Soc.*, 93(7), S25–S26, doi:10.1175.

700 Mears, C., J. Wang, D. Smith, and F. J. Wentz, 2015: Intercomparison of total precipitable
701 water measurements made by satellite- borne microwave radiometers and ground-
702 based GPS instruments. *J. Geophys. Res. Atmos.*, 120, 2492–2504,
703 doi:10.1002/2014JD022694.

704 Mears C., S.-P. Ho, L. Peng, and J. Wang, 2017): Total Column Water Vapor, [In “State
705 of the Climate in 2016]. *Bul. Amer. Meteor. Sci.*, **98** (8), S93–S98,
706 doi:10.1175/2017BAMSSStateoftheClimate.1.

707 Milz, M., S. A. Buehler, and V. O. John, 2009: Comparison of AIRS and AMSU-B
708 monthly mean estimates of upper tropospheric humidity, *Geophys. Res. Lett.*, L10804,
709 doi:10.1029/2008GL037068.

710 Neiman, P. J., F. M. Ralph, G. A. Wick, Y.-H. Kuo, T.-K. Wee, Z. Ma, G. H. Taylor, and
711 M. D. Dettinger, 2008: Diagnosis of an intense atmospheric river impacting the Pacific
712 Northwest: Storm summary and offshore vertical structure observed with COSMIC
713 satellite retrievals. *Mon. Wea. Rev.*, 136, 4398–4420.

714 Noël, S., M. Buchwitz, and J. P. Burrows, 2004: First retrieval of global water vapour
715 column amounts from SCIAMACHY measurements, *Atmos. Chem. Phys.*, 4, 111–
716 125.

717 Palm, M., C. Melsheimer, S. Noel, J. Notholt, J. Burrows, and O. Schrems, 2008: Integrated
718 water vapor above Ny Alesund, Spitsbergen: a multisensor intercomparison. *Atmos.*
719 *Chem. Phys. Discuss.* 8, 21171–21199.

720 Pougatchev, N., T. August, X. Calbet, T. Hultberg, O. Oduleye, P. Schlüssel, B. Stiller, K.
721 St. Germain, and G. Bingham, 2009: IASI temperature and water vapor retrievals –
722 error assessment and validation. *Atmos. Chem. Phys.*, 9, 6453–6458.

723 Prasad, A. K. and R. P. Singh, 2009: Validation of MODIS Terra, AIRS, NCEP/DOE
724 AMIP-II Reanalysis-2, and AERONET Sun photometer derived integrated precipitable
725 water vapor using ground-based GPS receivers over India. *J. Geophys. Res.*, 114,
726 D05107, doi:10.1029/2008JD011230.

727 Roman, J., R. Knuteson, and S. Ackerman, 2014: Time-to-detect trends in precipitable
728 water vapor with varying measurement errors. *J. Climate*, 27, 8259-8275.

729 Scherllin-Pirscher, B., C. Deser, S.-P. Ho, C. Chou, W. Randel, and Y.-W. Kuo, 2012:
730 The vertical and spatial structure of ENSO in the upper troposphere and lower
731 stratosphere from GPS radio occultation measurements, *Geophys. Res. Lett.*, 39,
732 L20801, 6 PP., 2012, doi:10.1029/2012GL053071.

733 Schliessel, P., & Emery, W. J. 1990: Atmospheric water vapour over oceans from SSM/I
734 measurements. *International Journal of Remote Sensing*, 11(5), 753-766.

735 Sherwood, S.C., W. Ingram, Y. Tsushima, M. Satoh, M. Roberts, P.L. Vidale and P.A.O.
736 Gorman, 2010: Relative humidity changes in a warmer climate. *J. Geophys. Res.*,
737 115, D09104, doi:10.1029/2009JD012585.

738 Soden, B. J., and J. R. Lanzante, 1996: An assessment of satellite and radiosonde
739 climatologies of upper-tropospheric water vapor. *Journal of Climate*, 9(6), 1235-
740 1250.

741 Soden, B. J., R. T. Wetherald, G. L. Stenchikov, and A. Robock, 2002: Global cooling after
742 the eruption of Mount Pinatubo: A test of climate feedback by water
743 vapor. *Science*, 296(5568), 727-730.

744 Sohn, B. J., and E. A. Smith, 2003: Explaining sources of discrepancy in SSM/I water
745 vapor algorithms. *J. Climate*, 16, 3229–3255, doi:10.1175/1520-
746 0442(2003)016<3229:ESODII.2.0.CO;2.

747 Soden, B.J. and I.M. Held, 2006: Assessment of climate feedbacks in coupled ocean-
748 atmosphere models. *J. Climate*, 19, 3354-3360.

749 Sohn, B.-J., and R. Bennartz, 2008: Contribution of water vapor to observational estimates
750 of longwave cloud radiative forcing, *J. Geophys. Res.*, 113, D20107,
751 doi:10.1029/2008JD010053.

752 Teng, W.-H., C.-Y. Huang, S.-P. Ho, Y.-H. Kuo, and X.-J. Zhou, 2013: Characteristics of
753 Global Precipitable Water in ENSO Events Revealed by COSMIC Measurements,
754 *J. Geophys. Research*, Vol. 118, 1–15, doi:10.1002/jgrd.50371.

755 Thompson, A., 2007: Simulating the adiabatic ascent of atmospheric air parcels using the
756 cloud chamber, Department of Meteorology, Penn State.

757 Trenberth K. E. and Guillemot, C. J., 1998: Evaluation of the atmospheric moisture and

758 hydrological cycle in the NCEP/NCAR reanalyses. *Clim. Dyn.*, 14:213–231

759 Trenberth, K.E., J. Fasullo, and L. Smith, 2005: Trends and variability in column

760 integrated atmospheric water vapor. *Climate Dynamics*, 24, 741–758.

761 Wang, J., L. Zhang, A. Dai, T. Van Hove, and J. Van Baelen, 2007: A near-global, 8-year,

762 2-hourly data set of atmospheric precipitable water from ground-based GPS

763 measurements. *J. Geophys. Res.*, 112, D11107, doi:10.1029/2006JD007529.

764 Wang, J and Zhang L. 2008: Systematic Errors in Global Radiosonde Precipitable Water

765 Data from Comparisons with Ground-Based GPS Measurements, *J. of Climate*, 21,

766 DOI:10.1175/2007JCLI1944.1.

767 Wang, L., X. Wu, M. Goldberg, C. Cao, Y. Li, and S.-H. Sohn, 2010: Comparison of AIRS

768 and IASI Radiances Using GOES Imagers as Transfer Radiometers toward Climate

769 Data Records. *J. Appl. Meteor. Climatol.* 49, 478–492.

770 Wick, G.A., Kuo, Y.-H., Ralph, F.M., Wee, T.-K., Neiman, P.J., Ma, Z, 2008:

771 Intercomparison of integrated water vapor retrievals from SSM/I and

772 COSMIC. *Geophys. Res. Lett.* 2008, 28, 3263–3266.

773 Wentz, F. J., 1997: A well-calibrated ocean algorithm for SSM/I. *J. Geophys.*

774 *Res.*, 102, 8703–8718.

775 Wentz, F. J., and R. W. Spencer, 1998: SSM/I rain retrievals within a unified all-weather

776 ocean algorithm. *J. Atmos. Sci.*, 56, 1613–1627.

777 Wentz, F. J., and M. Schabel, 2000: Precise climate monitoring using complementary

778 satellite data sets, *Nature*, 403, 414–416.

779 Wentz, F.J., Lucrezia Riccardulli, K. Hilburn, and C. Mears, 2007: How much more rain

780 will global warming bring? *Science*, 317, 233–235.

781 Wentz, F. J., 2013: SSM/I version-7 calibration report. *Remote Sensing Systems Tech.*
782 Rep. 011012, 46 pp.

783 Wentz, F. J. 2015: A 17-Year climate record of environmental parameters derived from
784 the Tropical Rainfall Measuring Mission (TRMM) microwave imager, *J. Clim.*,
785 doi:10.1175/JCLI-D-15-0155.1.

786 Yang, S., and X. Zou, 2012: Assessments of cloud liquid water contributions to GPS RO
787 refractivity using measurements from COSMIC and CloudSat. *J. Geophys. Res.*,
788 117, D06219, doi:10.1029/2011JD016452.

789 Zeng, Z., S.-P. Ho, S. Sokolovskiy, 2012: The Structure and Evolution of Madden-Julian
790 Oscillation from FORMOSAT-3/COSMIC Radio Occultation Data, *J. Geophys.*
791 *Research*, 117, D22108, doi:10.1029/2012JD017685.

792 Zou, X., S. Yang, and P. S. Ray, 2012: Impacts of ice clouds on GPS radio occultation
793 measurements. *J. Atmos. Sci.*, 69, 3670–3682.

794
795
796
797
798
799
800
801
802
803

804

805

806 Table 1. Satellite Instruments Used in This Study

807

Satellite	Instrument	Operation period
DMSP F15	SSM/I	December 1999-present
DMSP F16	SSMIS	October 2003-present
DMSP F17	SSMIS	December 2006-present
Coriolis	WindSat	February 2003-present

808

809

810

811

812

813

814

815

816

817

818

819

820

821

822

823

824

825

826

827

828 Table 2: Mean and standard deviation of differences (MW minus RO) in TPW (in mm)
829 between four MW radiometers and COSMIC RO under various sky conditions. The
830 sample numbers for each pair are shown in the third position of each column.
831

Sky condition	Mean/ σ /N			
	F15	F16	F17	WindSat
Clear	0.06/1.65/3064	0.03/1.47/3551	0.07/1.47/2888	0.18/1.35/1802
Cloudy	0.80/1.92/23614	0.79/1.73/29059	0.82/1.76/28403	0.96/1.73/20194
Non Precip	0.49/1.69/17223	0.46/1.46/21854	0.47/1.49/21371	0.49/1.36/13004
Precip	1.64/2.28/6391	1.83/2.05/7205	1.88/2.08/7032	1.85/2.00/7190

840

841

842

843

844

845

846

847

848

849

850

851

852

853

854

855

856

857

858

859

860

861

862

863

864

865

866

867

868
 869
 870
 871
 872
 873
 874
 875
 876
 877
 878
 879
 880
 881

Table 3: Mean and standard deviation (std) of the mean in mm of the monthly time series of differences of MW minus RO TPW under various sky conditions. The trend of the RO estimates of TPW in mm/decade and the 95% confidence level are shown below the mean and σ values in each row.

Sky condition	Mean/ σ of monthly time series RO trend (95% confidence levels indicated in ())			
	F15	F16	F17	WindSat
Clear	0.07/0.56 1.65 (0.47,2.84)	0.05/0.28 1.09 (-0.28,2.46)	0.08/0.27 0.21 (-1.22,1.65)	0.23/0.38 -0.12 (-1.89,1.66)
Cloudy	0.77/0.51 1.49 (0.40,2.58)	0.78/0.18 2.02(0.87,3.16)	0.82/0.15 1.85 (0.64,3.06)	0.95/0.17 1.85 (0.68,3.01)
Non Precipitation	0.46/0.48 0.86 (-0.24,1.95)	0.45/0.17 2.02 (0.87,3.17)	0.48/0.15 2.37 (1.23,3.50)	0.47/0.19 2.12 (0.95,3.30)
Precipitation	1.62/0.69 2.52 (0.55,4.480)	1.81/0.31 1.32 (-0.53,3.17)	1.88/0.29 0.26 (-1.59,2.10)	1.88/0.32 0.39 (-1.25,2.04)

882
 883
 884
 885
 886
 887
 888
 889
 890
 891
 892
 893
 894

895

896 Figure Captions

897

898 Figure 1. a.-e: The RSS V7.0 monthly mean F16 SSM/I a) TPW (in mm), b) surface skin
899 temperature (in K), c) liquid water path (LWP, in mm), and d) rain rate (RR, in
900 mm/hour), and e) distribution of matches of COSMIC RO and F16, F17, and WindSat
901 estimations of TPW used in this study.

902

903 Figure 2. TPW scatter plots for the COSMIC and RSS Version 7.0 pairs under clear
904 conditions for a) F15, b) F16, c) F17, and d) WindSat.

905

906 Figure 3. TPW scatter plots for the COSMIC and RSS Version 7.0 F16 SSM/I pairs
907 under a) cloudy, b) cloudy but non-precipitation, and c) precipitation conditions.

908

909 Figure 4. TPW scatter plots for the gb-GPS and RSS Version 7.0 F16 SSM/I pairs from
910 June 2006 to December 2013 under a) clear, b) cloudy, c) cloudy but non-precipitation,
911 and d) precipitation conditions.

912

913 Figure 5. Mean and standard of the mean for the F16-COSMIC TPW biases varying with
914 a) wind speed (m/s), b) TPW (mm), c) rain rate (mm/hour), d) total cloud water (mm),
915 and e) surface skin temperature (K). The vertical black bracket superimposed on the
916 mean denotes the standard error of the mean. The green dashed line is the number of
917 samples, indicated by the scale on the right.

918

919 Figure 6. Mean and standard of the mean for the F16- gb-GPS TPW biases varying with
920 a) wind speed (m/s), b) TPW (mm), c) rain rate (mm/hour), d) total cloud water (mm) and
921 e) surface skin temperature (K). The vertical black bracket superimposed on the mean
922 denotes the standard error of the mean. The green dashed line is the number of samples,
923 indicated by the scale on the right.

924

925 Figure 7. The time series of monthly mean F16 – COSMIC TPW differences under a)
926 clear, b) cloudy, c) cloudy but non-precipitation, and d) precipitation conditions. The
927 black line is the mean difference for microwave radiometer minus COSMIC; the vertical
928 lines superimposed on the mean values are the standard error of the mean. The number of
929 the monthly MW radiometer- COSMIC pairs is indicated by the green dashed line (scale
930 on the right Y axis).

931

932 Figure 8. The time series of de-seasonalized TPW differences (microwave radiometer –
933 COSMIC) under cloudy skies for a) F15, b) F16, c) F17, d) WindSat. The black line is
934 the mean difference for microwave radiometer minus COSMIC; the vertical lines
935 superimposed on the mean values are the standard error of the mean. The number of the
936 monthly MW radiometer- COSMIC pairs is indicated by the green dashed line (scale on
937 the right Y axis). The trends are shown by solid red line. The 95% confidence intervals
938 for slopes are shown in the parentheses.

939

940 Figure 9. The de-seasonalized time series of monthly mean TPW for all MW and
941 COSMIC observations under all sky conditions. The red and blue dashed lines are the
942 best fit of de-seasonalized COSMIC and MW TPW time series, respectively.

943

944 Figure 10. The global map of TPW trend in mm/decade over oceans using all F16, F17,
945 WindSat data from 2006 to 2013.

946

947 Figure 11. Global mean TPW monthly anomaly (mm) relative to 1981-2010 mean for
948 ocean regions 60°S-60°N from ERA-Interim reanalysis (green), RSS microwave (blue) and
949 COSMIC (red). (Based on data from Mears et al., 2017).

950

951

952

953

954

955

956

957

958

959

960

961

962

963

964

965

966

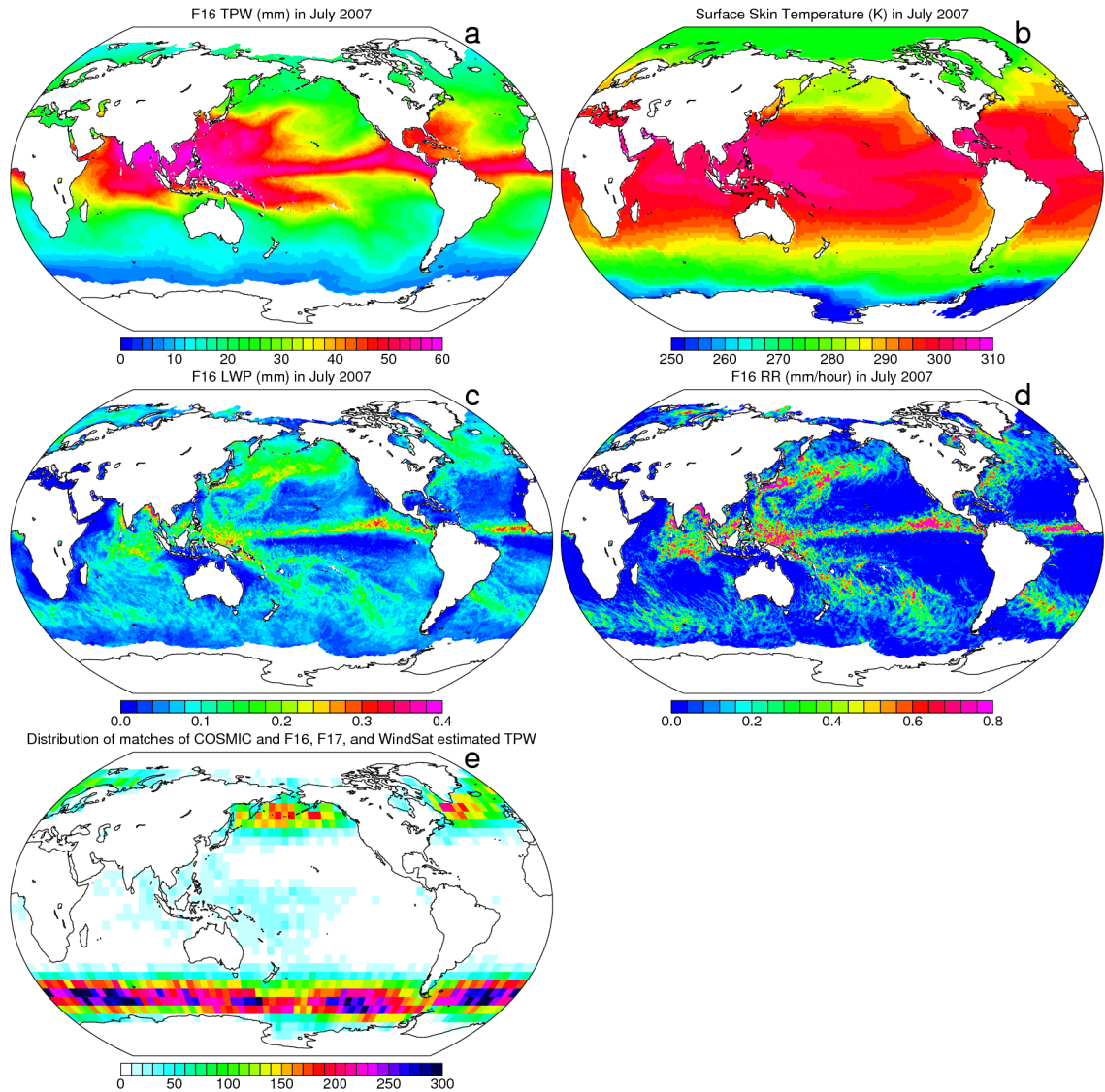
967

968

969

970

971
972

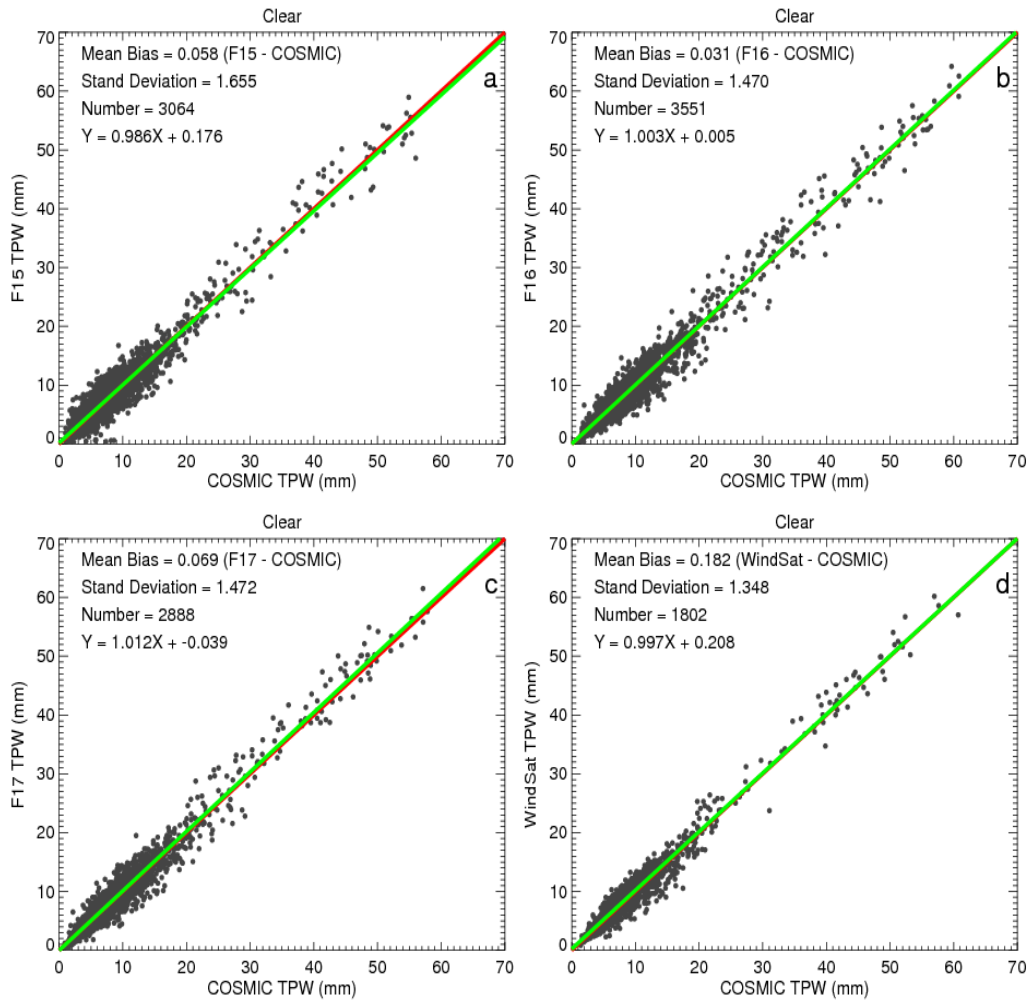


973
974
975
976
977
978
979
980
981
982

Figure 1. a-e: The RSS V7.0 monthly mean F16 SSM/I a) TPW (in mm), b) surface skin temperature (in K), c) liquid water path (LWP, in mm), d) rain rate (RR, in mm/hour), and e) distribution of matches of COSMIC RO and F16, F17 and WindSat estimations of TPW used in this study.

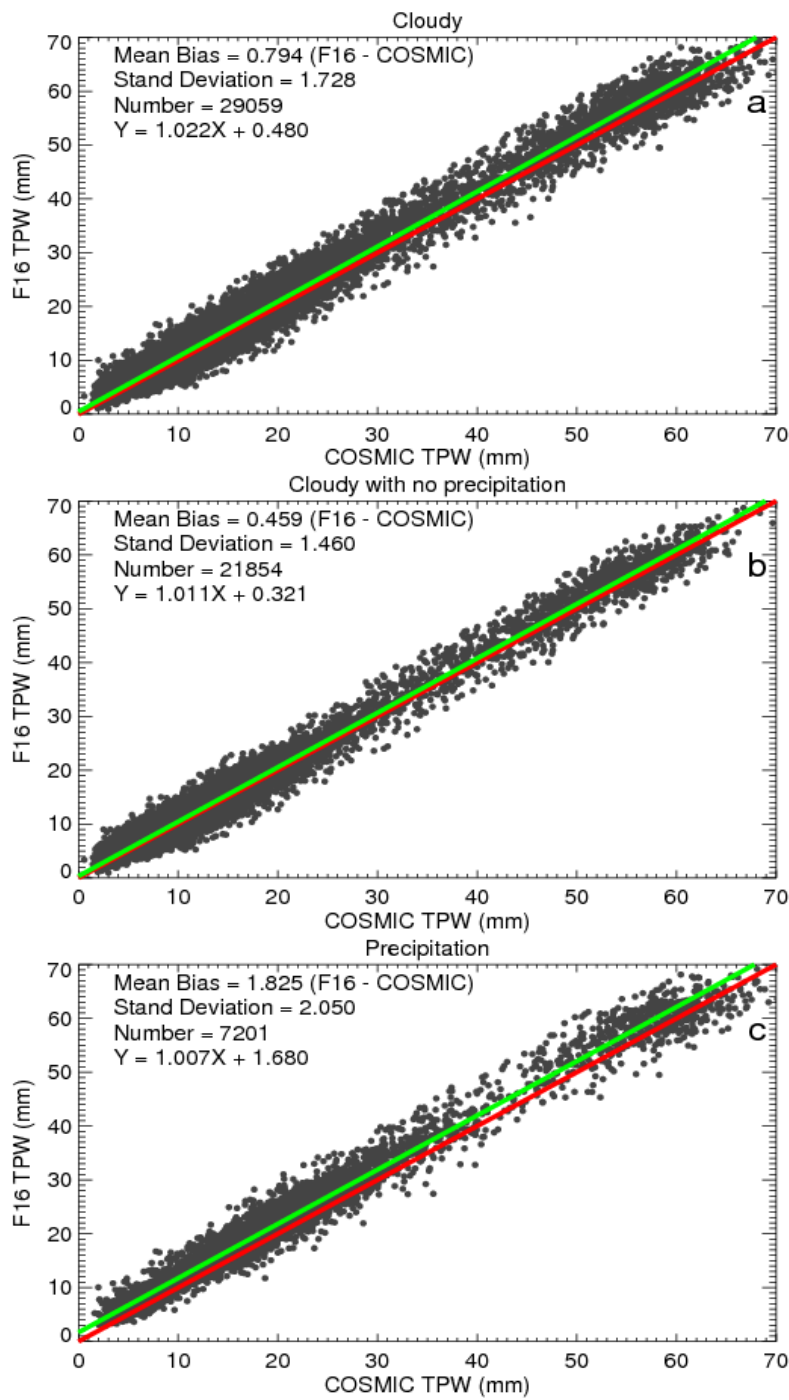
983
984
985

986
987
988



989
990
991
992
993
994
995
996
997
998
999

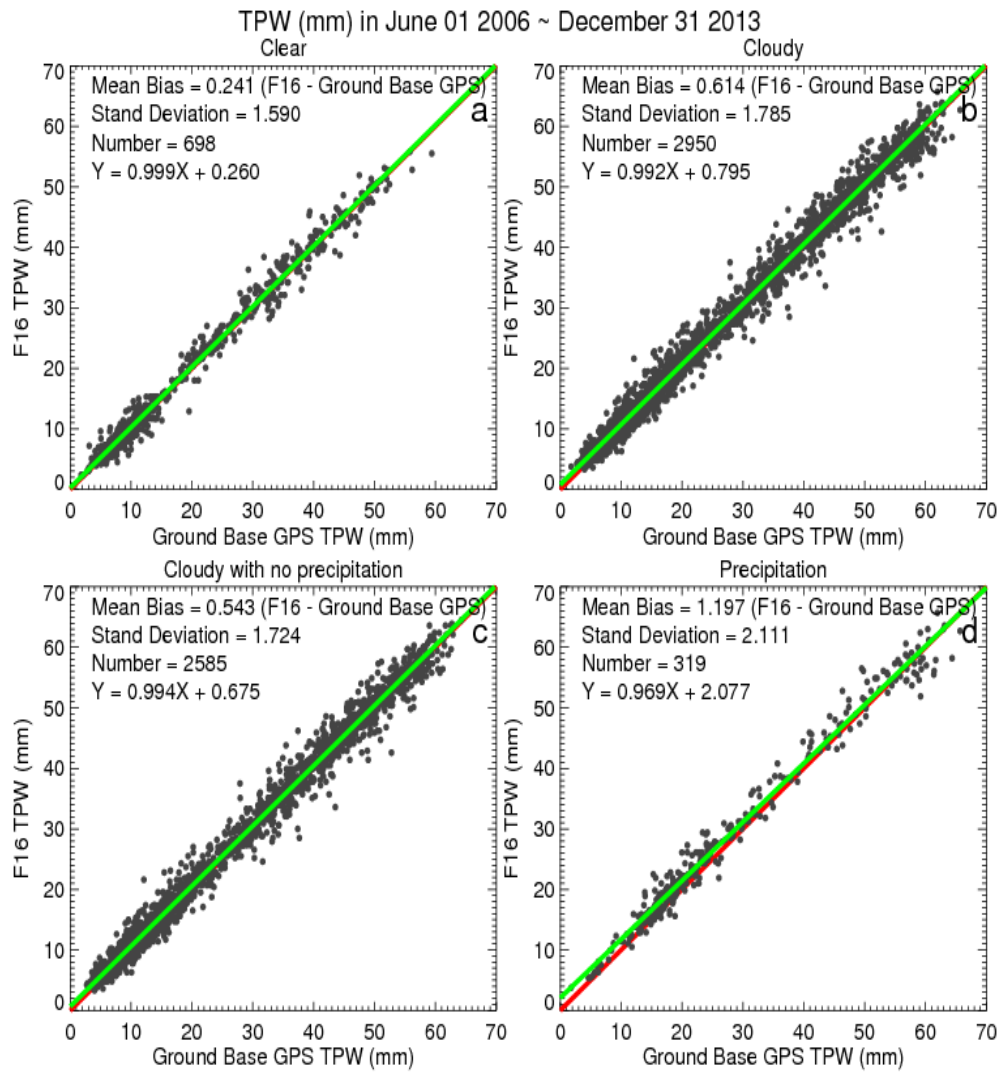
Figure 2. TPW scatter plots for the COSMIC and RSS Version 7.0 pairs under clear conditions for a) F15, b) F16, c) F17, and d) WindSat.



1000
 1001
 1002
 1003
 1004
 1005
 1006
 1007

Figure 3. TPW scatter plots for the COSMIC and RSS Version 7.0 F16 SSM/I pairs under a) cloudy, b) cloudy but non-precipitation, and c) precipitation conditions.

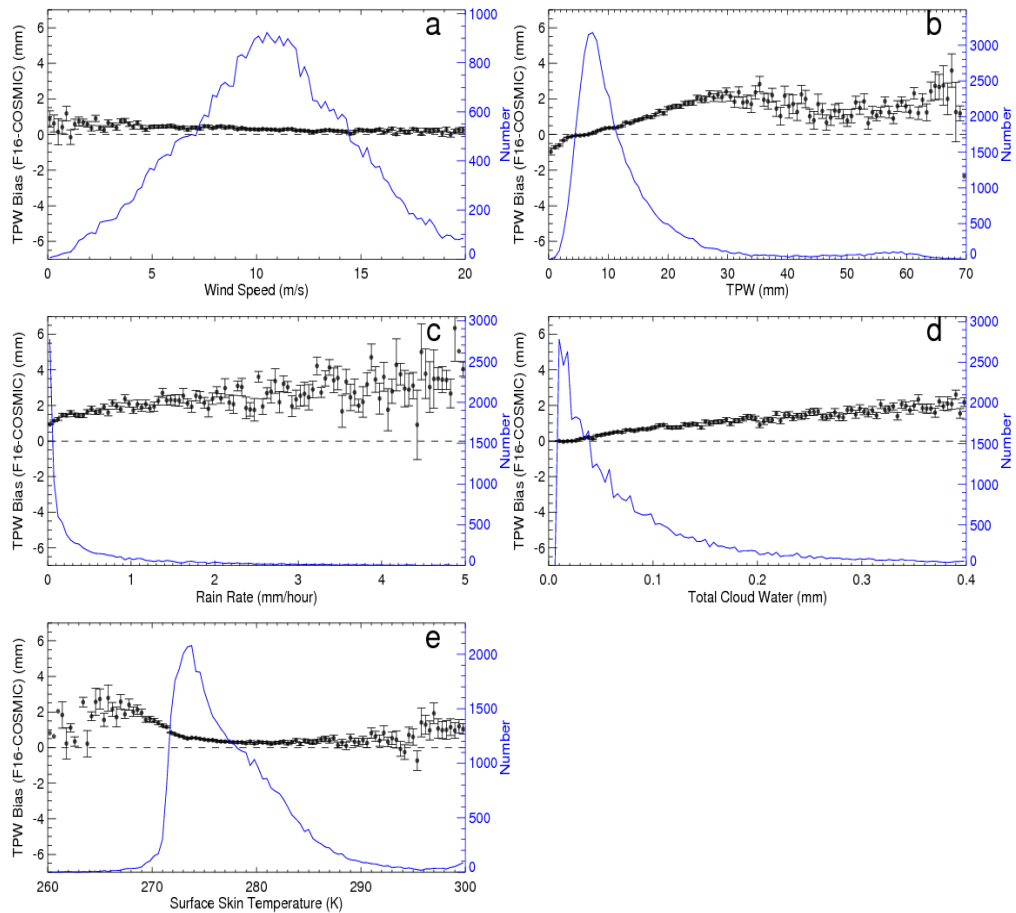
1008
1009



1010
1011
1012
1013
1014
1015
1016
1017
1018
1019
1020
1021
1022
1023
1024
1025

Figure 4. TPW scatter plots for the gb-GPS and RSS Version 7.0 F16 SSM/I pairs from June 2006 to December 2013 under a) clear, b) cloudy, c) cloudy but non-precipitation, and d) precipitation conditions.

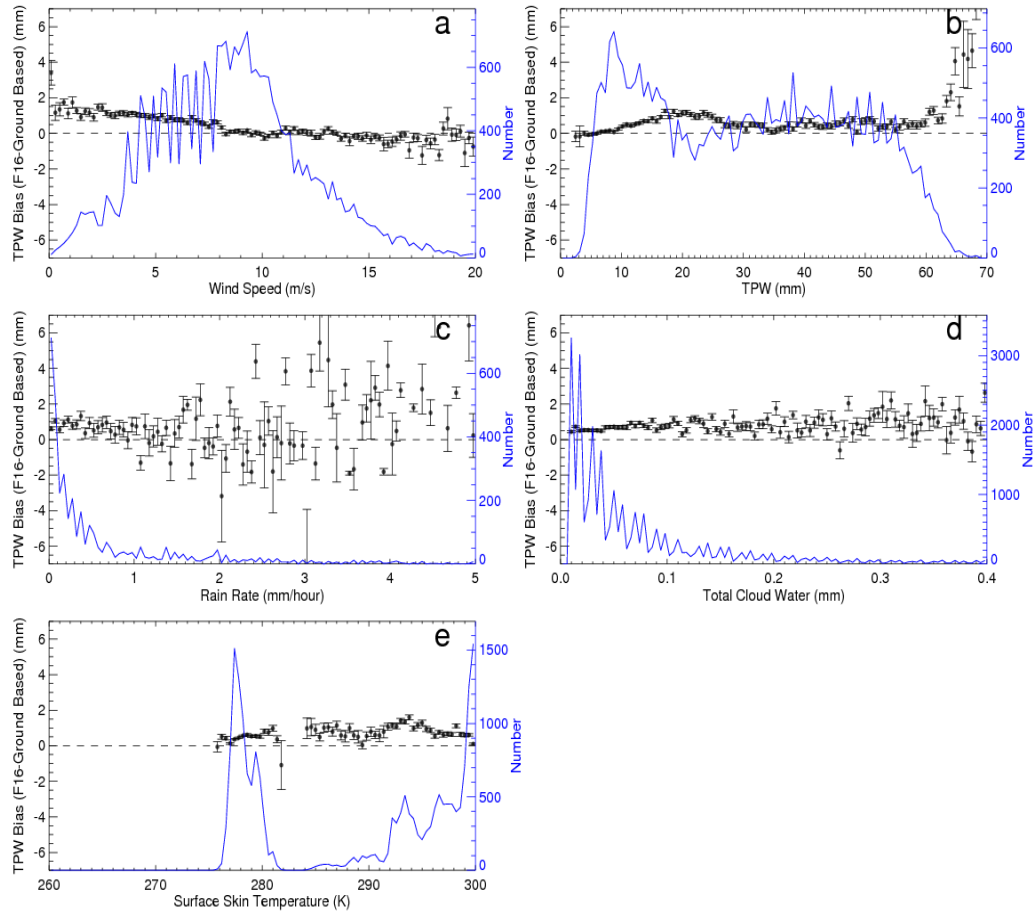
1026
1027



1028
1029
1030
1031
1032
1033
1034
1035
1036
1037
1038
1039
1040
1041
1042
1043
1044
1045
1046
1047

Figure 5. Mean and standard of the mean for the F16-COSMIC TPW biases varying with a) wind speed (m/s), b) TPW (mm), c) rain rate (mm/hour), d) total cloud water (mm), and e) surface skin temperature (K). The vertical black bracket superimposed on the mean denotes the standard error of the mean. The green dashed line is the number of samples, indicated by the scale on the right.

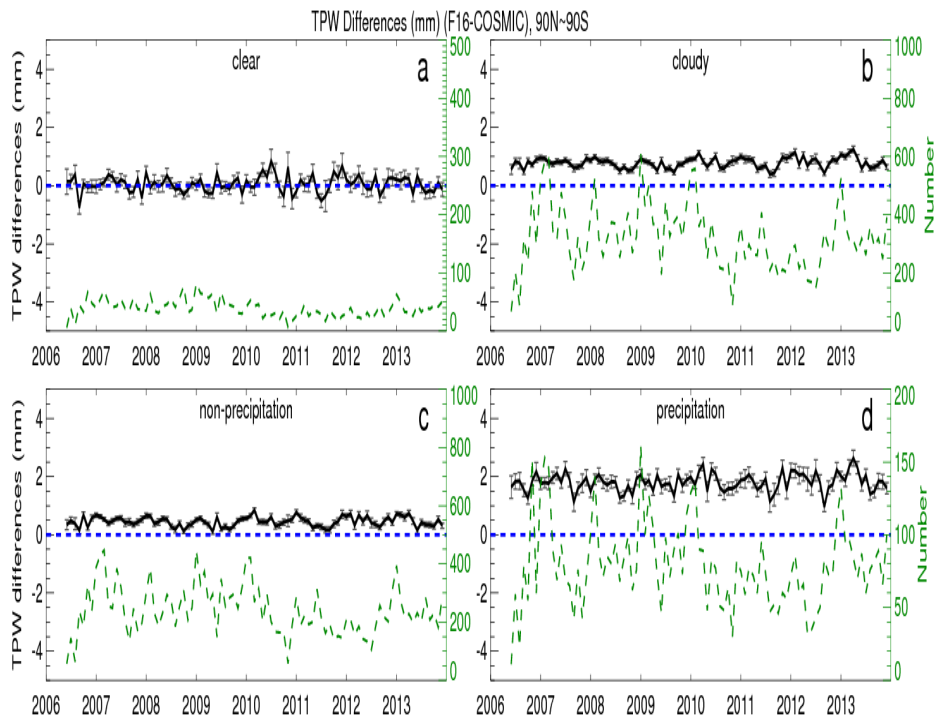
1048
1049
1050
1051
1052



1053
1054
1055
1056
1057
1058
1059
1060
1061
1062
1063
1064
1065
1066
1067
1068
1069

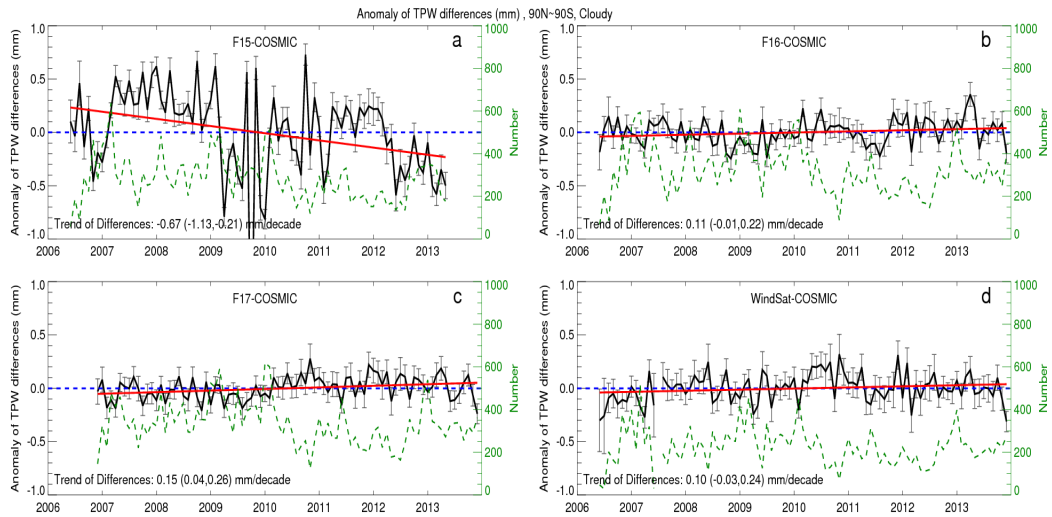
Figure 6. Mean and standard of the mean for the F16- gb-GPS TPW biases varying with a) wind speed (m/s), b) TPW (mm), c) rain rate (mm/hour), d) total cloud water (mm) and e) surface skin temperature (K). The vertical black bracket superimposed on the mean denotes the standard error of the mean. The green dashed line is the number of samples, indicated by the scale on the right.

1070
1071
1072



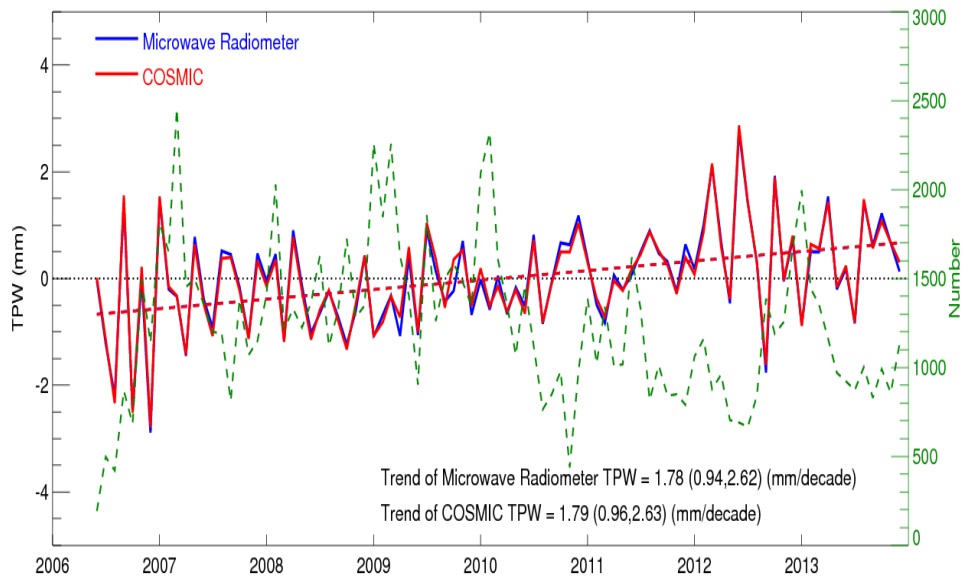
1073
1074
1075
1076
1077
1078
1079
1080
1081
1082
1083
1084
1085
1086
1087

Figure 7. The time series of monthly mean F16 – COSMIC TPW differences under a) clear, b) cloudy, c) cloudy but non-precipitation, and d) precipitation conditions. The black line is the mean difference for microwave radiometer minus COSMIC; the vertical lines superimposed on the mean values are the standard error of the mean. The number of the monthly MW radiometer- COSMIC pairs is indicated by the green dashed line (scale on the right Y axis).



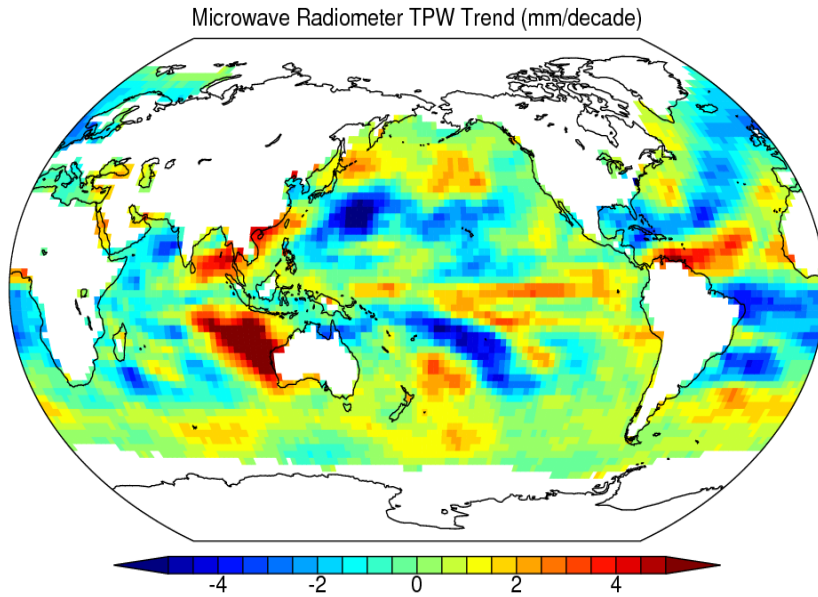
1088
 1089
 1090
 1091
 1092
 1093
 1094
 1095
 1096
 1097
 1098
 1099
 1100
 1101
 1102
 1103
 1104
 1105
 1106
 1107
 1108
 1109
 1110
 1111
 1112

Figure 8. The time series of de-seasonalized TPW differences (microwave radiometer – COSMIC) under cloudy skies for a) F15, b) F16, c) F17, d) WindSat. The black line is the mean difference for microwave radiometer minus COSMIC; the vertical lines superimposed on the mean values are the standard error of the mean. The number of the monthly MW radiometer- COSMIC pairs is indicated by the green dashed line (scale on the right Y axis). The trends are shown by solid red line. The 95% confidence intervals for slopes are shown in the parentheses.



1113
 1114
 1115
 1116
 1117
 1118
 1119
 1120
 1121
 1122
 1123
 1124
 1125
 1126
 1127
 1128
 1129
 1130
 1131
 1132
 1133
 1134
 1135
 1136

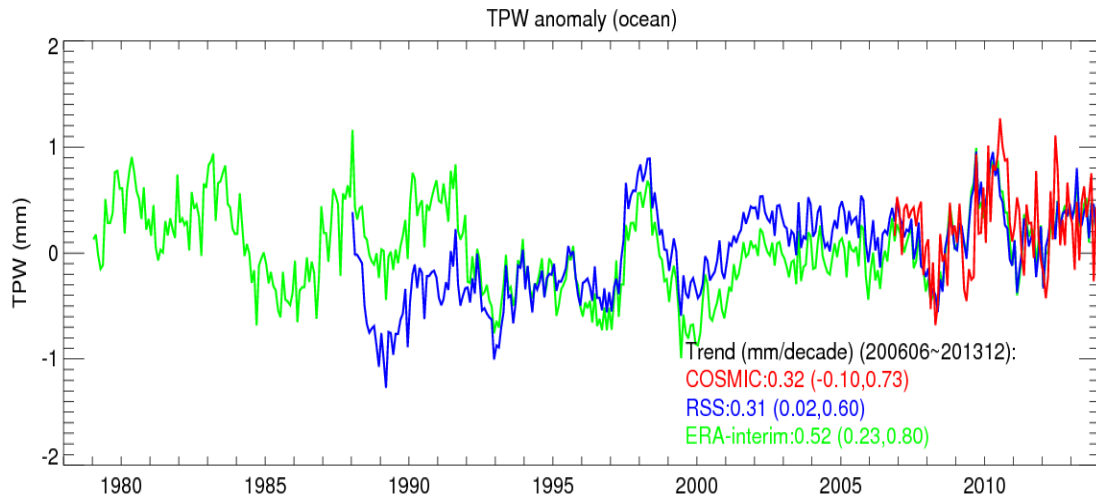
Figure 9. The de-seasonalized time series of monthly mean TPW for all MW and COSMIC observations under all sky conditions. The red and blue dashed lines are the best fit of de-seasonalized COSMIC and MW TPW time series, respectively.



1137
1138
1139
1140
1141
1142

Figure 10. The global map of TPW trend in mm/decade over oceans using all F16, F17, WindSat data from 2006 to 2013.

1143
1144
1145
1146
1147
1148
1149
1150



1151

1152

1153 Figure 11. Global mean TPW monthly anomaly (mm) relative to 1981-2010 mean for
 1154 ocean regions 60°S-60°N from ERA-Interim reanalysis (green), RSS microwave (blue) and
 1155 COSMIC (red). (Based on data from Mears et al., 2017).